

1 (Submitted version)

2 Miocene cave sediments record topographic, erosional and
3 drainage development in the Western European Alps
4

5 François Lemot^{a,*}, Pierre G. Valla^a, Peter van der Beek^b, Marianna Jagercikova^c, Samuel
6 Niedermann^d, Julien Carcaillet^a, Edward R. Sobel^b, Sergio Andò^e, Eduardo Garzanti^e,
7 Xavier Robert^a, Mélanie Balvay^a, Matthias Bernet^a, Johannes Glodny^d

8 ^a*Institut des Sciences de la Terre (ISTerre), Université Grenoble Alpes, Université Savoie Mont Blanc, CNRS, IRD, IFSTTAR, Grenoble, France*

9 ^b*Institut für Geowissenschaften, Universität Potsdam, Potsdam-Golm, Germany*

10 ^c*St. Maurice en Valgodemard, France*

11 ^d*GFZ German Research Centre for Geosciences, Potsdam, Germany*

12 ^e*Department of Earth and Environmental Sciences, University of Milano Bicocca, Milano, Italy*

13
14 *Correspondence: francois.lemot@univ-grenoble-alpes.fr
15

16 **Keywords:**

17 *Western European Alps, Exhumation and uplift history, Drainage network, Sediment provenance,*
18 *Cave sediment record, Cosmogenic nuclides burial dating, Detrital thermochronology*

19 **Abstract**

20 The dynamic Neogene evolution of the Western European Alps included exhumation of the external
21 crystalline massifs, thrust propagation to the foreland, drainage network reorganization, and major
22 climatic variations. To constrain possible interactions between those factors, accurate
23 geomorphological and sedimentological archives are required. However, intra-orogenic areas are
24 subject to erosion and extensive glacial cover during the Quaternary erased most of the geomorphic
25 markers in the Alps. For these reasons, the genesis of the main features of the modern landscape, such
26 as the major valleys and the drainage network, remains poorly understood. This study highlights how
27 recently discovered karstic archives from the perched paleo-karst of the Obiou peak (Dévoluy massif,
28 SE France) record the tectonic and drainage-network evolution of this part of the Alps during the
29 Neogene. The Obiou caves are located at 2250-2380 m elevation, ~1600 m above the Drac valley; they
30 contain fluvial deposits including sand-clay units and rounded crystalline cobbles derived from the
31 adjacent Ecrins-Pelvoux massif. As the Dévoluy and Ecrins-Pelvoux massifs are currently separated by

32 the axial Drac valley (a major tributary of the Isère River), these cave sediments must have been
33 deposited by a radial drainage system before incision of the modern Drac. We report new multi-
34 method results from these sediments, including cosmogenic-nuclide burial dating (^{21}Ne , ^{10}Be , ^{26}Al in
35 quartz), provenance analysis (clast petrography and heavy-mineral analysis), and detrital
36 thermochronology (apatite fission-track and (U-Th)/He) combined with a paleo-environmental
37 reconstruction from palynology. $^{21}\text{Ne}/^{10}\text{Be}$ dating of cobbles and sand constrains the burial age to 11.5
38 ± 1.5 Ma, providing a maximum age for the modern axial drainage system and a minimum long-term
39 incision rate of ~ 140 m/My for the Drac valley. Comparison of the combined data to both modern
40 rivers and nearby Oligocene foreland-basin deposits provides evidence for two successive drainage
41 reorganisations. Early Miocene exhumation and development of high topography in the Ecrins-Pelvoux
42 massif, linked to localised thrusting on a crustal-scale ramp, led to initial deflection of the antecedent
43 radial drainage network, beheading its headwaters by establishment of the axial upper Durance valley.
44 Subsequent propagation of thrusting into the subalpine Dévoluy massif and associated uplift during
45 the mid to late Miocene led to establishment of the modern drainage system.

46

47 1. Introduction

48 The fluvial drainage network sets the base level and ensures the redistribution and evacuation
49 of water and sediment fluxes generated upstream in mountain belts. The efficiency of transport
50 processes along the drainage network therefore limits erosional fluxes, controlling topographic
51 development and *in fine* the balance between uplift and denudation (*Whipple et al., 1999*). Changes
52 in drainage patterns influence sediment deposition in basins (e.g., *Kuhlemann et al., 2006; Allen, 2008*)
53 and can affect evolution and biodiversity (e.g., *Craw et al., 2016*). The current drainage pattern of the
54 Western European Alps appears suboptimal in its function; as several trunk rivers, including the Rhône,
55 Rhine, and Isère, flow parallel to the axis of the orogen, and therefore perpendicular to its overall
56 gradient, for an extended part of their course (Fig. 1A). The origin of such axial drainage, which
57 contrasts to the more common radial drainage pattern, has been a major question in geomorphology
58 for decades (e.g., *Oberlander and Morisawa, 1985*). In the French Western Alps, the initiation and
59 timing of incision of the near-continuous axial Isère and Drac valleys, locally known as the “*Sillon*
60 *Subalpin*”, have been discussed since the middle of the last century (e.g., *Blanchard, 1947; Debelmas,*
61 *1995*). However, none of the evolutionary scenarios proposed (involving river capture, glacial incision,
62 or gravitational collapse) satisfactorily explain the current drainage pattern.

63 Fluvial drainage reconstructions based on the sedimentary record imply that the early
64 Miocene drainage system of the European Alps was mostly radial (*Schlunegger et al., 1998; Kuhlemann*
65 *et al., 2006; Jourdan et al., 2012*), suggesting major drainage reorganization during the Neogene. The
66 transition time between these two drainage configurations remain to be elucidated, as do the potential
67 links to the topographic evolution and the driving mechanisms for these changes. The main Alpine axial
68 valleys are systematically located adjacent to the External Crystalline Massifs (ECM), where the highest
69 topography and present-day uplift rates in the mountain range are found (*Sternai et al., 2019* and
70 references therein). The ECM started uplifting and exhuming during the early Miocene (*van der Beek*
71 *et al., 2010; Glotzbach et al., 2011a; Herwegh et al., 2019; Valla et al., 2021*). This spatial and temporal
72 coincidence raises the prospect of an integrated geodynamic model to link tectonics, topographic
73 development, and drainage reorganization in the Western European Alps.

74 To this aim, reliable geomorphic and sedimentological archives are required, but extensive
75 Quaternary glaciations and valley incision (e.g., *Valla et al., 2011*) have erased most of these markers
76 within the mountain belt, while foreland-basin sediments (e.g., *Kuhlemann and Kempf, 2002;*
77 *Glotzbach et al., 2011b*) only provide range-scale integrated records. Karstic systems may, however,
78 host remarkable archives and are particularly well suited to studying the relief history of mountain
79 ranges. In particular, several studies have related cave elevations to paleo-base levels and used
80 terrestrial cosmogenic nuclide (TCN) dating to recover past fluvial incision rates in various contexts
81 (e.g., *Granger et al., 1997; Haeuselmann et al., 2007; McPhillips et al., 2016; Sartégou et al., 2018*).
82 Complementary data from karstic archives, such as thermochronology or petrography, can provide key
83 information about sediment provenance and/or paleo-exhumation rates (*Sauro et al., 2021*). However,
84 the quantitative analysis of karstic archives is challenging due to limitations in the TCN dating methods
85 (*Ma et al., 2018*), often limited cave preservation and access, and the potential complexity of the karst
86 system (*Malcles et al., 2020*).

87 Here, we use a multi-method approach to characterize Alpine-basement derived sediments
88 that were recently discovered in caves of the Dévoluy massif, SE France (*Jagercikova et al., 2021; Fig.*
89 *1B, C*). We present new ^{26}Al - ^{10}Be - ^{21}Ne burial dating, detrital apatite fission-track (AFT) and apatite (U-
90 Th-Sm)/He (AHe) thermochronology, petrographic and heavy-mineral data. Combined with previously
91 published pollen analyses (*Jagercikova et al., 2022*), these data are used to propose a consistent model
92 for the Miocene topographic, erosional and river-drainage development of the French Western Alps.

93 2. Geological and morphological setting

94 The European Alps result from the collision between Europe and Adria that has been ongoing
95 since the early Paleogene, and are composed of a number of tectonic units corresponding to different
96 paleogeographic domains and metamorphic facies. The western European Alps contain two major
97 units: the external zones, corresponding to the former European rifted margin, and the internal zones,
98 corresponding to the former Piedmont-Ligurian Ocean and Briançonnais continental sliver (e.g., *Masini*
99 *et al.*, 2013). The internal zones have undergone subduction-related metamorphism during the Eocene
100 (*Rosenbaum and Lister, 2005*), whereas the external zones exhibit only very low-grade Alpine
101 metamorphism (*Bellanger et al.*, 2015). The external zones comprise basement units of the External
102 Crystalline Massifs (ECM), overlain by Mesozoic marly and calcareous sediments that have been folded
103 and faulted to form the Subalpine massifs, and Cenozoic synorogenic molasse deposits (Fig. 1).

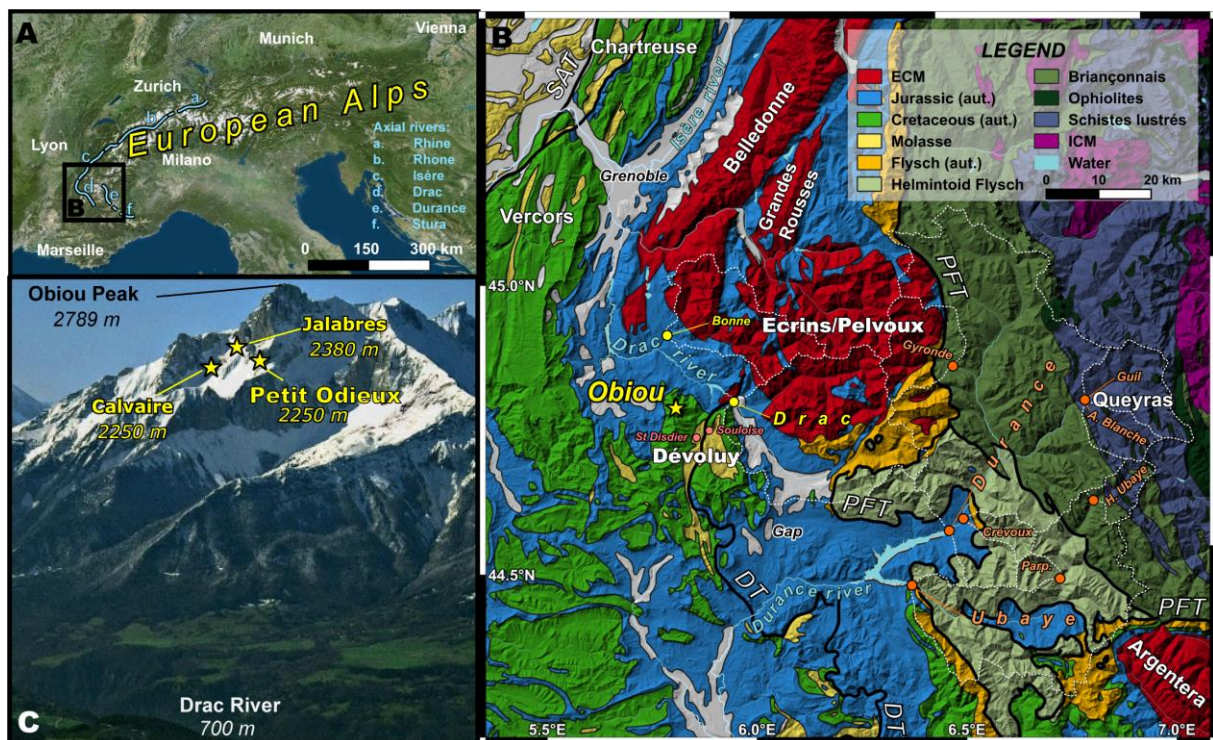
104 Several observations allow reconstructing the Alpine tectonic evolution of the External
105 crystalline massifs; more specifically in the scope of this study, the Ecrins-Pelvoux Massif (Fig. 1). The
106 deposition of Late-Eocene (Priabonian; 38-34 Ma) flysch, known as the Champsaur sandstone, on a
107 paleo-topography (*Gupta and Allen, 2000*) implies that basement rocks were locally at the surface
108 during that period. Subsequent tectonic burial under overthrust internal-zone units and thickening
109 related to shortening led to low-grade metamorphic conditions, as recorded by phengite formation in
110 shear zones dated by $^{40}\text{Ar}/^{39}\text{Ar}$ to between 34 and 25 Ma (*Simon-Labric et al.*, 2009; *Bellanger et al.*,
111 2015). Paleomagnetism and zircon fission-track (ZFT) thermochronometry record an onset of
112 exhumation for the Ecrins-Pelvoux massif between 30 and 24 Ma (*Crouzet et al.*, 2001; *van der Beek et*
113 *al.*, 2010), with basement rocks that are currently at the surface being exhumed through the apatite
114 fission-track (AFT) closure depth of around 4 km between 10 and 3 Ma (*Seward et al.*, 1999; *van der*
115 *Beek et al.*, 2010; *Beucher et al.*, 2012). During Miocene times, thrusting and shortening propagated to
116 the Subalpine massifs (*Philippe et al.*, 1998; *Girault et al.*, 2022; *Bilau et al.*, *in review*). In the Vercors
117 and Chartreuse massifs (Fig. 1), syn-tectonic deposition of molasse sediments in front of the active
118 thrusts records southeast-to-northwest propagation of deformation between the Burdigalian (20-16
119 Ma) and the Pliocene (*Kalifi et al.*, 2022). The major thrusts of the Subalpine massifs disappear
120 southwest of the Pelvoux massif, where another structure, the Digne thrust sheet, accommodated
121 shortening during Miocene times (*Schwartz et al.*, 2017; Fig. 1B).

122 In contrast to their geodynamic and tectonic evolution, the morphologic and topographic
123 development of the western European Alps remain much less understood. The Oligocene to lower
124 Miocene molasse deposited in the Subalpine massifs contains detritus derived from the internal zones
125 of the Alps (*Bocquet, 1966; Meckel, 1997; Jourdan et al.*, 2012), attesting to the existence of a radial

126 drainage network extending into the internal zones. At that time, high topography appears to have
 127 been restricted to the internal zones (Fauquette et al., 2015). This pattern strongly contrasts with the
 128 current situation where the external zones, in particular the ECM, host the highest topography with
 129 major peaks (e.g., Mont Blanc: 4808 m; Barre des Ecrins: 4102 m), and mark a secondary drainage
 130 divide that is only crossed by a few large rivers (e.g., the Isère River northeast of the Belledonne
 131 massif).

132

133

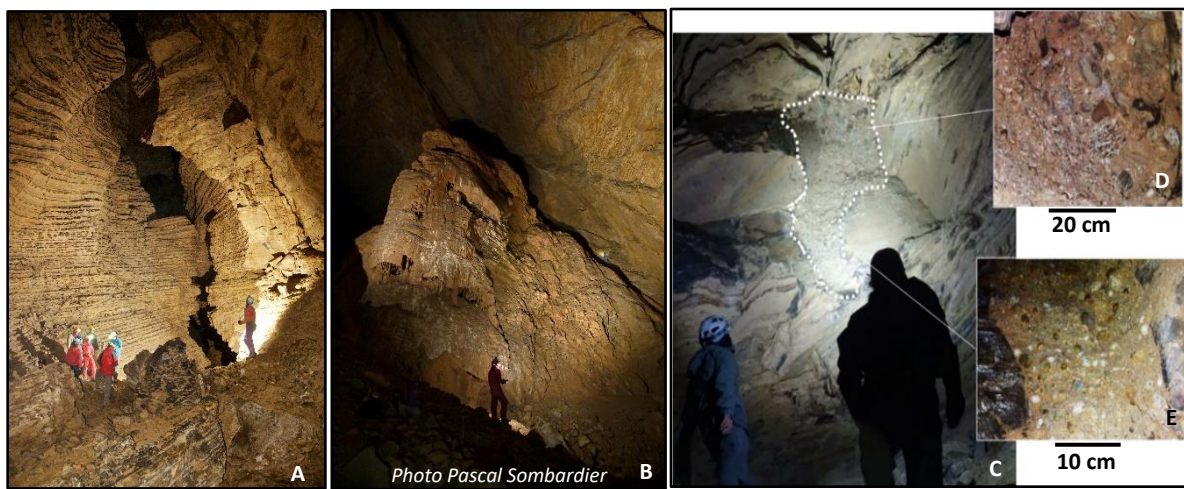


134

135 **Figure 1:** Location and setting of the studied Obiou caves. **A:** Satellite image (source:
 136 <https://www.geoportail.gouv.fr/>) showing the location of the study area in the western European Alps (black
 137 square indicates extent of panel B). The major axial valleys of the Western Alps are highlighted with blue lines.
 138 **B:** Regional geological map with the main tectonic units discussed in the text (*ECM*: external crystalline massif;
 139 *ICM*: internal crystalline massif; *aut.*: autochthonous) and the major Alpine thrusts (thick black lines; *DT*: Digne
 140 thrust; *PFT*: Penninic frontal thrust; *SAT*: Sub-Alpine thrust). The names of the main massifs are indicated in bold
 141 white font. The location of the Obiou caves is indicated with a yellow star, and other sand samples used in this
 142 study are shown by colored circles (yellow: modern rivers – this study; orange: modern rivers – published data;
 143 pink: Dévoluy molasse) with the corresponding river catchments outlined by white dashed lines. **C:** North face of
 144 the Obiou peak with the entrances of the three studied caves (yellow stars).

145

146 The Subalpine Dévoluy massif is located southwest of the Ecrins-Pelvoux massif (Fig. 1), and is
147 characterized by thick Upper-Cretaceous limestones with a high karstification potential. We studied
148 three fossil caves (the Jalabres, Petit Odieux, and Calvaire caves) located on the northeast flank of the
149 Obiou peak between 2250 and 2380 m elevation, ~1600 m above the modern Drac River (Fig. 1). These
150 caves are disconnected from the present-day drainage network and were not connected to other
151 massifs during Quaternary glaciations (*Monjuvent, 1978*). This high-mountain paleo-karst system
152 preserves alluvial sediments that include abundant crystalline cobbles, indicating non-local sediment
153 sources and fluvial transport (*Jagercikova et al., 2021*).



154 **Figure 2:** Morphology of the Jalabres cave (see location in Fig. 1B, C). **A:** Sub-horizontal paleo-meander incising
155 into limestone units. **B:** 60-m high dome with massive speleothem attesting of past warm conditions. **C-D-E:**
156 Alluvial deposits with sandy material and crystalline cobbles preserved as an infilled sediment pocket within the
157 paleo-meander (panel A).

158

159 The Jalabres cave, situated at 2380 m elevation, is a 200-m long horizontal cave preserving a
160 30-m high paleo-meander (Fig. 2A). The canyon shape and large volume of the main karstic gallery
161 indicate that karstification occurred in the vadose zone with high water discharge (*Audra and Palmer,*
162 *2011*). The cave ends abruptly on a fault, which borders a voluminous 60-m high collapsed dome. A
163 >10-m high speleothem, located at the inner extremity of the cave (Fig. 2B), testifies of past warmer
164 conditions, as the modern mean annual temperature of 1 °C in the cave prevents such massive calcite
165 precipitation. Crystalline cobbles intermixed with a sand and clay matrix have been found *in situ* at
166 different sites that are elevated above the cave floor (Fig. 2C). They indicate possible complete
167 sediment filling of the cave, which may have protected it from collapse after disconnection from the
168 local base level (i.e., the Drac River, Fig. 1). The alluvial material analyzed in this study was collected
169 from two sites: the first consists of collapsed conglomerates including crystalline pebbles and cobbles

170 interbedded with mica-rich sands and clays; and the second site is a pocket infilled with sand, pebbles,
171 and cobbles (Fig. 2C-D-E). Locally derived components such as chert or limestone are rare in these
172 outcrops, implying the absence of mixing between these *in-situ* alluvial sediments and autochthonous
173 material.

174 The Petit Odieux cave, located at 2250 m elevation, has developed horizontally along a
175 stratification level in the limestone units. Its total volume is much smaller than that of the Jalabres
176 cave (the cave is roughly 1-m high at the outcrop of allochthonous sediment), and its morphology is
177 more anastomosing. The floor of the Petit Odieux cave is covered with conglomerates, including
178 products of cave ceiling collapse, allochthonous elements (sand and pebbles), and reworked salmon-
179 colored calcified clays. A section of laminated clays was found *in-situ* in a small infill and was collected
180 for pollen analysis (*Jagercikova et al., 2022*). Because of the sediment filling and posterior cave
181 collapses, the original section of the gallery is unknown. Finally, the Calvaire cave, also located at 2250
182 m elevation, displays even more degraded outcrops and sediment infills including some angular blocks
183 of sandstone that are composed of reworked allochthonous sand in a calcitic cement. The collected
184 sediment infill is located near the cave entrance.

185 3. Methods

186 Our analysis focused on determining the depositional age of the cave sediments, identifying
187 their provenance, and using them to infer paleo-exhumation rates of the source area(s). Cosmogenic
188 ^{21}Ne - ^{10}Be - ^{26}Al burial dating (e.g., *Granger and Muzikar, 2001; Niedermann, 2002*) was used to constrain
189 the timing of deposition. For provenance analysis, we used pebble counting combined with sand
190 petrography and heavy-mineral analysis (e.g., *Garzanti and Andò, 2019*). Detrital apatite fission-track
191 (AFT) and (U-Th-Sm)/He (Ahe) thermochronology of cave sediments was used to infer the exhumation
192 history of the source area (e.g., *Glotzbach et al., 2011b*).

193 3.1 TCN burial dating

194 To ensure reproducibility, four samples were collected in the Jalabres cave for TCN burial
195 dating, including one individual cobble (JAL20-01), one pebble mixture (JAL20-06), and two sand
196 samples (JAL20-07, JAL20-08). The first two samples were collected from the infill shown in Fig. 2C-E,
197 whereas the sand samples derive from a site closer to the entrance of the Jalabres cave (site 1 of
198 *Jagercikova et al., 2021*). We included two indurated samples from the other caves: a calcite-cemented
199 sandstone rich in crystalline elements collected near the entrance of the Calvaire cave (CAL20-01), and
200 crystalline cobbles from conglomerates in the Petit Odieux cave (YEUX20-01).

201 Samples were prepared at the ISTERre GTC platform (University Grenoble Alpes, France). After
202 preliminary crushing of cobble and pebbles, all samples were sieved to extract the 100-800 μm
203 fraction. Quartz was separated using a Frantz[®] isodynamic magnetic separator and purified through
204 chemical dissolution in successive baths of H_2SiF_6 and HCl . Purified quartz was etched three times in
205 HF to remove possible contaminations of atmospheric ^{10}Be .

206 For ^{10}Be and ^{26}Al analyses, quartz fractions were spiked with 500 μl of a 998.0 ± 3.5 ppm Be carrier
207 (Scharlau Batch 16107901) for ^{10}Be concentration determination and dissolved with concentrated HF
208 solution. The natural ^{27}Al concentrations in the samples were measured on a Varian 720 ES ICP-AES at
209 the ISTERre Geochemistry platform using the 396.152 nm emission line. ^{10}Be and ^{26}Al extraction
210 followed the conventional procedure of *Merchel and Herpers (1999)*. $^{10}\text{Be}/^9\text{Be}$ and $^{26}\text{Al}/^{27}\text{Al}$ ratios were
211 measured at the French National AMS facility ASTER (CEREGE, Aix-en-Provence, France; *Arnold et al.,*
212 *2010*) using for calibration the in-house Be standard (*Braucher et al., 2015*), the assumed $^{10}\text{Be}/^9\text{Be}$ ratio
213 of which is 1.191×10^{-11} . Correction for a full-process blank ratio of $^{10}\text{Be}/^9\text{Be} = 7.62 \times 10^{-15}$ was applied.
214 For $^{26}\text{Al}/^{27}\text{Al}$ we measured an analytical blank ratio of 1.05×10^{-15} .

215 ^{21}Ne measurements were performed on 0.7-1.1 g of HF -etched quartz aliquots of the Jalabres
216 cave samples at the GFZ Potsdam (Germany), following methods described in *Niedermann (2002)* and
217 *Hetzel et al. (2002)*. The abundance of cosmogenic ^{21}Ne was determined by stepwise heating at 400,
218 600, 800, and 1200°C, and computed assuming a two-component mixture of cosmogenic and trapped
219 Ne in the 400-800°C steps, with trapped Ne having either atmospheric composition or the composition
220 determined by in-vacuo crushing of aliquots of the quartz samples (Table S2). This method allows to
221 detect nucleogenic contributions or compositions dominated by isotopic mass fractionation
222 (*Niedermann, 2002*). Aliquots of the quartz standard CREU-1 that were measured during the sample
223 batch yielded a ^{21}Ne excess of $340 \pm 14 \times 10^6$ at g^{-1} and $345.8 \pm 7.4 \times 10^6$ at g^{-1} , respectively,
224 consistent with the reference value $348 \pm 10 \times 10^6$ at g^{-1} (*Vermeesch et al., 2015*).

225 The calculation of burial ages relies on an assumed production rate, which is strongly
226 dependent on the paleo-elevation, especially for slowly-eroding settings (e.g., *Granger and Muzikar,*
227 *2001; Blard et al., 2019*). Production rates were estimated with the scaling model of *Lal (1991)* and the
228 global ^{10}Be sea-level-high-latitude production rate of 4.1 ± 0.2 at $\text{g}^{-1} \text{y}^{-1}$ (*Martin et al., 2017*). The effect
229 of latitude change is negligible at this timescale compared to other uncertainties, particularly for the
230 estimated production rate. We considered only neutron spallation that produces ^{21}Ne and ^{10}Be with a
231 ratio of 4.2 ± 0.2 (*Kober et al. 2011*).

232 3.2. Petrography

233 The petrography of pebbles and sand samples was analyzed and systematically compared with
234 sediments of nearby rivers that drain regions of known lithologies (Fig. 1B). The lithology of n randomly
235 picked pebbles (diameter 1 to 10 cm) was analyzed for the Jalabres cave (JAL20-04, $n=130$) and two
236 modern rivers draining the southwest part of Pelvoux massif: the Drac River ($n=113$) and the Bonne
237 River ($n=93$; sampling locations indicated in Fig. 1B).

238 Sand petrography was investigated for a sandstone sample from the Calvaire cave (CAL20-01),
239 a conglomerate matrix and a sand sample from the Petit Odieux cave (YEUX20-05, YEUX20-13), and a
240 sand sample from the Jalabres cave (JAL20-04). Sands were classified according to the proportions of
241 the three main groups of framework components (Q: quartz; F: feldspar; L: lithic fragments),
242 considered where exceeding 10% QFL and listed in order of abundance (e.g., in a feldspatho-quartzo-
243 lithic sand $L>Q>F>10\%$ QFL; *Garzanti, 2019*). Rock fragments were classified by protolith composition
244 and metamorphic rank.

245 From a split aliquot of the 15-500 μm size window obtained by wet sieving, heavy minerals
246 were separated by centrifuging in Na-polytungstate (density 2.90 g/cm^3) and recovered by partial
247 freezing with liquid nitrogen (Andò, 2020). For each sample, ≥ 200 transparent heavy minerals (tHM)
248 were point-counted at an appropriate regular spacing (200 or 300 μm ; *Garzanti and Andò, 2019*).
249 Opaque minerals, rock fragments, iron oxides, soil clasts, phyllosilicates and carbonates were not
250 considered as integral parts of the tHM suite. The same analysis was performed on two samples
251 representative of the two main local formations making up the Dévoluy Molasse: the uppermost
252 Eocene-lowermost Oligocene Souloise and lower Oligocene Saint-Disdier sandstones (*Meckel, 1997*).
253 New data from modern sands from the Bonne and Drac rivers and literature data for rivers draining
254 the internal Alps (*Garzanti et al., 2010*) were used for comparison. All sample sites are indicated on
255 Figure 1B.

256 3.3. AFT and AHe thermochronology

257 In addition to samples JAL20-01, JAL20-06, JAL20-07, JAL20-08, CAL20-01, and YEUX20-01,
258 which were also analyzed for TCN burial dating, we included a pebble mix from the Jalabres cave
259 (JAL20-09) for thermochronological analysis. Apatite grains were separated from the 160-250 μm
260 fraction using standard heavy-liquid and magnetic separation techniques. Apatite aliquots were hand-
261 picked and mounted in epoxy resin, polished and etched with 5.5 M HNO_3 for 20 s at 21 °C. Apatite
262 mounts were covered with muscovite sheets as external detectors and irradiated together with
263 dosimeter glass IRMM 540R at the FRM II Research Reactor in Munich (Germany) along with Durango

264 standards. After irradiation, mica detectors were etched in 48% HF at 21 °C for 18 minutes. Fission
265 tracks were counted at the ISTERre GTC platform by M. Balvay using the ζ -calibration approach
266 (*Hurford and Green, 1983*). Track lengths were measured whenever possible, as well as etch-pit widths
267 (Dpar values) that can be used as kinetic indicators. Apatite grains for AHe analysis were hand-picked
268 from Jalabres-cave samples and measured at the ISTERre GTC platform. AHe analysis was performed
269 at the University of Potsdam (He degassing and measurement) and GFZ Potsdam (U, Th, and Sm
270 measurements) following the methodology described in *Zhou et al. (2017)*.

271 4. Results

272 4.1. TCN burial dating

273 Concentrations of cosmogenic ^{10}Be and ^{21}Ne in quartz for all cave sediments are reported in
274 Table 1. Detailed information and full analytical data are available in the Supplementary material
275 (Tables S1-S2). All measured ^{26}Al concentrations were below the analytical blank, whereas ^{10}Be
276 concentrations were all significantly above the measured blank. We noticed a strong granulometric
277 effect among JAL samples (Table 1): sand samples (JAL20-07 and -08) have a higher ^{10}Be concentration
278 than pebbles (JAL20-06), and pebbles have a higher ^{10}Be concentration than the cobble (JAL20-01).
279 These differences may be due to different erosion processes before burial, as cobbles and pebbles may
280 be derived from landslides and thus have been brought abruptly to the surface (e.g., *Mariotti et al.,*
281 *2019*). The cosmogenic ^{21}Ne abundance was computed both as the excess relative to the fluid-inclusion
282 composition (as determined by crushing extractions; Table S2) and relative to air for samples JAL20-
283 06, JAL20-07 and JAL20-08; those samples plot along the spallation line in a Ne three-isotope diagram
284 (Fig. 3A), and they provide similar concentrations of cosmogenic ^{21}Ne . Sample JAL20-01 shows very
285 little ^{21}Ne excess and its data can essentially be explained by mass fractionation; thus, the nominal
286 cosmogenic ^{21}Ne concentration reported in Table 1 should be taken as a maximum estimate.

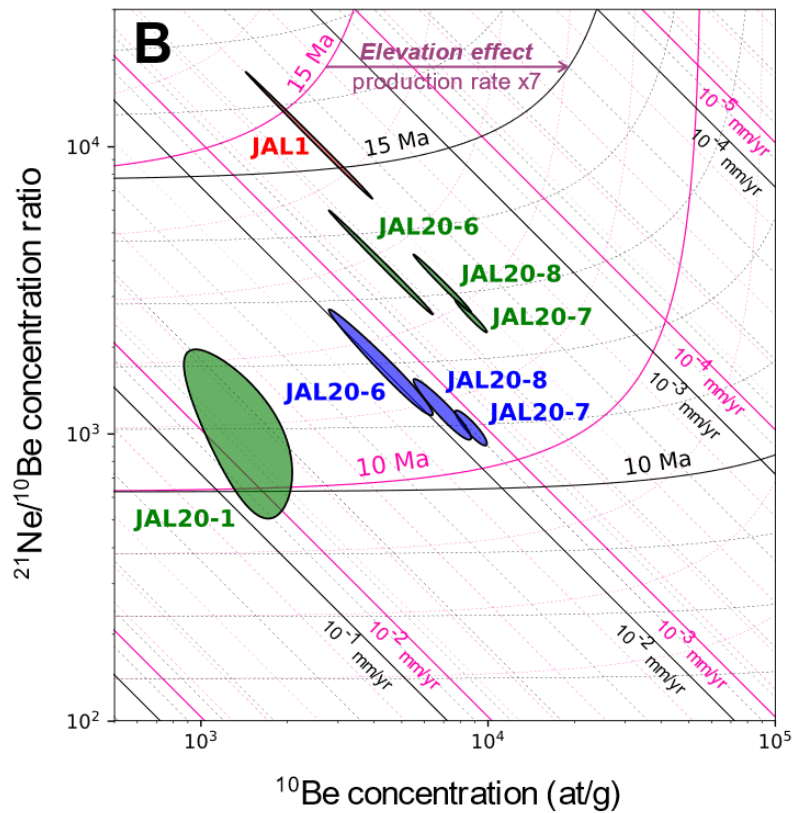
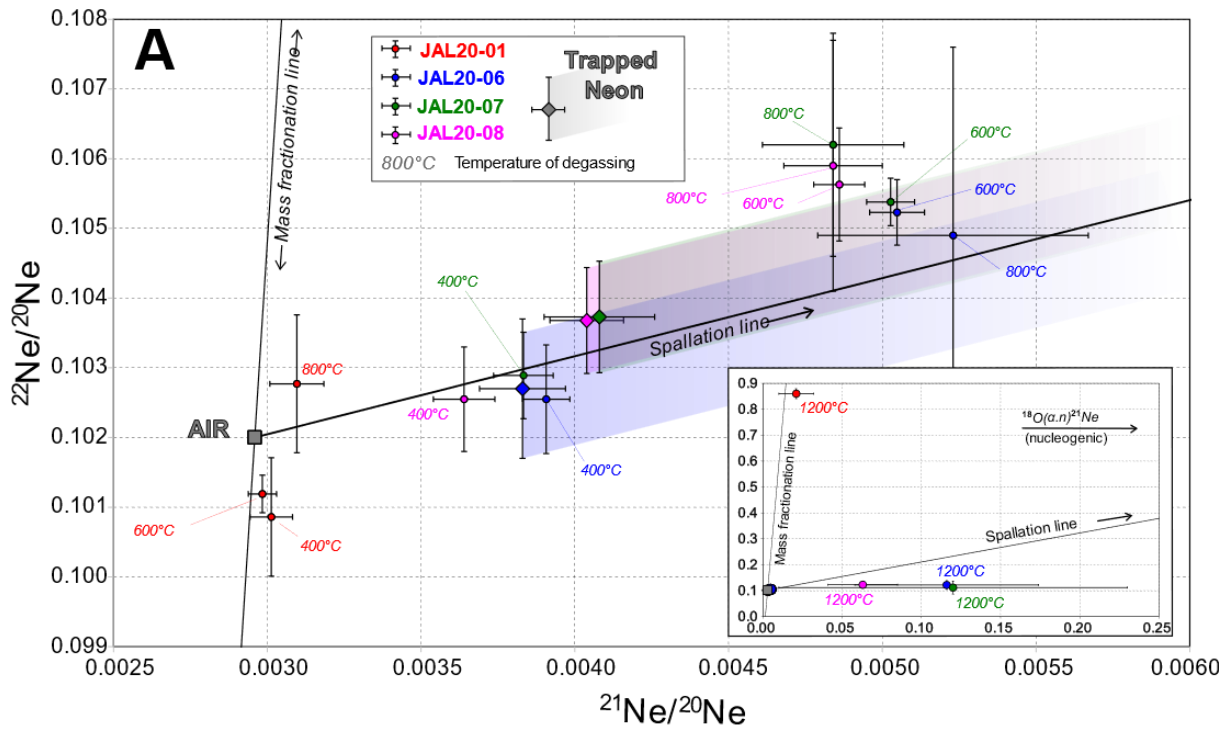
287 $^{10}\text{Be}/^{21}\text{Ne}$ burial plots (Fig. 3B) provide a convenient way to represent this relationship (e.g.,
288 *Ma et al., 2018; Blard et al., 2019*). To assess the burial-age dependence on production rates, isochrons
289 and iso-erosion lines are plotted for two end-member scenarios: a scaling factor of 1 corresponding to
290 a sea-level paleo-production rate (pink lines), and of 7 considering a paleo-elevation of approximately
291 2.5 km (black lines). Between those two end-member scenarios, paleo-erosion rates are directly
292 affected by the 7-fold difference in paleo-production rates, but the burial-age estimates are robust,
293 with <1 Ma variation between the two considered scenarios. Considering all analytical uncertainties,
294 the different estimates of cosmogenic ^{21}Ne concentration, and the paleo-elevation effect on
295 production rates, our best-estimate $^{10}\text{Be}/^{21}\text{Ne}$ burial ages range from 10.5 to 13 Ma. This is younger
296 than, but overlaps within error bars, a previous estimate based on a single sample from the Jalabres

297 cave (15.6 ± 3.8 Ma; *Jagercikova et al., 2021*). The difference is due to a much higher ^{21}Ne
 298 concentration measured in the previous study in which only a single-step extraction was performed at
 299 1500°C , potentially linked to some contribution of nucleogenic neon trapped in fluid inclusions.

300

Sample	Grain size (cm)	Quartz mass for ^{10}Be extraction (g)	^{10}Be ($\times 10^3$ at/g)	^{21}Ne excess relative to air ($\times 10^6$ at/g)	^{21}Ne excess relative to trapped component ($\times 10^6$ at/g)
JAL20-01	13 cm	74.6	2.0 ± 0.6	$1.5^{+0.7}_{-0.4}$	Not measured
JAL20-06	2 – 10 cm	30.0	5.7 ± 1.8	16.4 ± 0.4	$7.4^{+0.6}_{-0.5}$
JAL20-07	100 – 800 μm	49.6	9.5 ± 1.1	22.0 ± 0.6	9.0 ± 0.6
JAL20-08	100 – 800 μm	14.7	9.5 ± 1.6	22.7 ± 0.6	8.3 ± 0.6

301 **Table 1:** Measured cosmogenic ^{10}Be and ^{21}Ne concentrations (with 1σ uncertainty) in quartz from samples from
 302 the Jalabres cave. See Tables S1 and S2 (Supplementary material) for full analytical details.

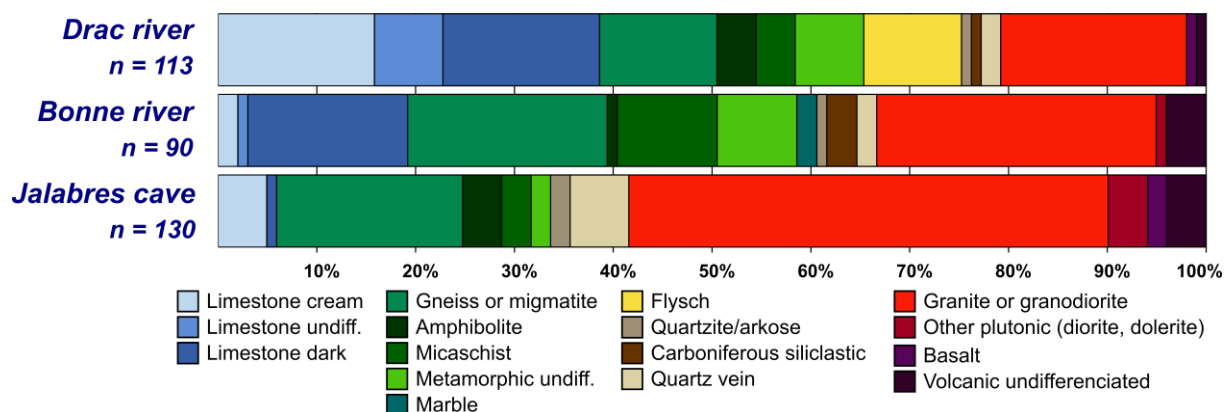


305 **Figure 3:** ^{10}Be and ^{21}Ne cosmogenic nuclide measurements and estimated burial ages for JAL samples. **A:** Ne
 306 isotopic ratios (2σ errors). A pure mixture of trapped atmospheric and cosmogenic Ne should lie on the spallation

307 line. Shaded areas correspond to a mix of a trapped component, as determined by crushing extractions, and
 308 cosmogenic neon. The neon released during the 1200 °C heating step was not considered as its composition
 309 suggests a nucleogenic origin (see inset for details). Data from sample JAL20-01 plot close to the mass
 310 fractionation line. **B:** Cosmogenic $^{10}\text{Be}/^{21}\text{Ne}$ burial plot with 1σ error ellipses. Cosmogenic ^{21}Ne is taken as the
 311 excess relative to the result of the crushing extraction (blue) and to air (green). A single previous analysis (JAL1)
 312 from *Jagercikova et al. (2021)*, for which ^{21}Ne excess was computed relative to air and extracted using a single
 313 degassing step at 1500 °C, is shown in red. Two end-member scenarios have been considered for production
 314 rates, affecting burial ages (curves) and paleo-erosion rates (lines): a scaling factor of 1 corresponding to a sea-
 315 level paleo-production rate (pink), and of 7 considering to 2.5-km paleo-elevation (black).

316 4.2. Petrography and provenance

317 Among the 130 pebbles counted from the sediment infill of the Jalabres cave (Fig. 4), 49% are
 318 granitoids, followed by gneiss (19%), vein quartz, amphibolite, volcanics, limestone, micaschist, and
 319 epidote-rich metamorphic rocks. In contrast, the modern Bonne River carries only 29% granitoid
 320 pebbles but 41% metamorphic rocks, including numerous meta-volcanics from the Taillefer/Pelvoux
 321 cortex zone. Liassic dark marls and limestones are also more abundant (16 %) than in the cave
 322 sediments. Modern Drac River deposits are even richer in sedimentary pebbles, with 39% limestone
 323 and 10% flysch (Champsaur sandstone, not found in the Jalabres cave but observed in marmot burrows
 324 near the entrance; *Jagercikova et al., 2021*); granitoids represent only 19% of the counted pebbles.
 325 Therefore, cave sediments appear representative of the Pelvoux basement, as currently sampled by
 326 the Bonne and Drac rivers, although granite is over-represented with respect to gneiss and crystalline
 327 rocks are over-represented with respect to sedimentary rocks, relative to modern river deposits. This
 328 difference may represent a bias due to transport length, as softer lithologies are preferentially
 329 removed downstream (e.g., *Dingle et al., 2017*). In contrast to the Dévoluy molasse (*Meckel, 1997*), no
 330 component derived from the internal Alps (such as serpentinite or radiolarite) was encountered in the
 331 Jalabres cave pebbles.



332 **Figure 4:** Comparison of pebble lithologies between the sedimentary infill of the Jalabres cave and modern
 333

334 sediments from rivers draining the Ecrins-Pelvoux massif. Number of counted pebbles - Jalabres: 130; Drac: 113;
335 Bonne: 90.

336

337 The sand fraction of the Jalabres cave sample is litho-feldspatho-quartzose with
338 metagranitoid (diorite, tonalite) and high-rank metamorphic grains including garnet amphibolite.
339 Volcanic lathwork and metapsammite grains also occur. The tHM suite, dominated by green-brown
340 hornblende with garnet and oxy-hornblende (Table S3; Fig. S1) is notably richer (tHM concentration
341 3.3% of bulk sample) than in modern sands of the Bonne (tHMC 0.4%) and Drac (tHMC 0.6%) Rivers.
342 Modern river sands have similar tHM suites dominated by blue-green hornblende with epidote; green
343 augite and garnet are common in the Drac sand, whereas apatite is common in the Bonne sand.

344 The Petit Odieux cave sediments consist of a matrix-supported conglomerate with granite,
345 gneiss, micaschist, dark sandstone, and volcanic clasts. The clasts and clays, potentially reworked in
346 the cave, are mixed with coarse sand with a petrographic composition similar to both adjacent sand
347 deposits within the Petit Odieux cave and the sandstone sample from the Calvaire cave. This
348 feldspatho-litho-quartzose sand contains low- to medium/high-rank metapelite, metapsammite, and
349 micritic or sparitic carbonate rock fragments. Plagioclase and orthoclase occur in subequal
350 proportions; biotite dominates over muscovite. Samples from the Petit Odieux and Calvaire caves have
351 poor tHM suites (tHMC 0.6 and 0.1%, respectively) that mainly contain apatite, epidote, garnet and
352 zircon; most of the dense fraction consists of Ti-oxides and Fe-hydroxides, with rare hematite.

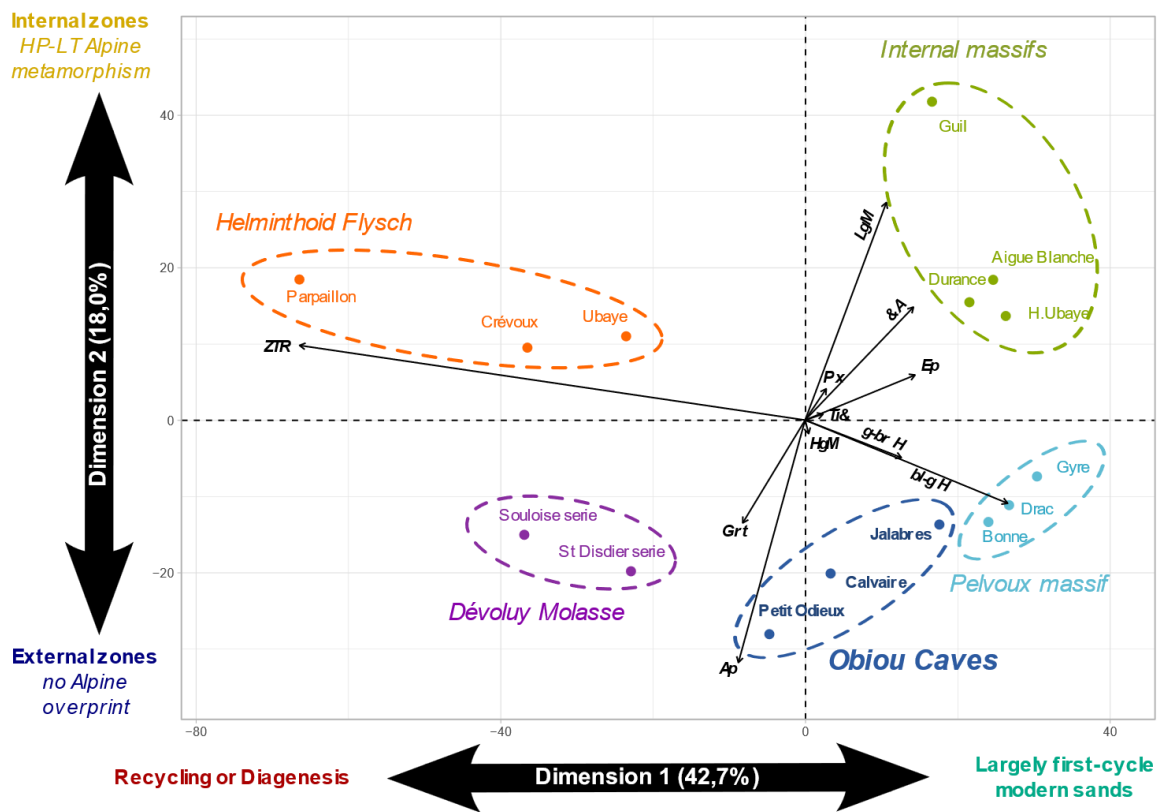
353 The Dévoluy molasse samples have a different mineralogy. The very fine-grained and
354 extensively calcified litho-quartzose Souloise sandstone contains plagioclase, slate lithics, muscovite,
355 and glauconite. The coarse-grained feldspatho-quartzo-lithic Saint Disdier sandstone contains
356 abundant serpentine schist and cellular serpentinite grains diagnostic of provenance from the Internal
357 Alps ophiolites (*Garzanti et al., 2010*), together with plagioclase, microlithic volcanic, chloritoschist,
358 slate, and metasandstone rock fragments. The tHM suite of both molasse samples is extremely poor
359 (tHMC 0.04-0.05%), with durable apatite, garnet, rutile, zircon, tourmaline, and minor Cr-spinel, but
360 no unstable ferromagnesian minerals. Garnet commonly shows corrosion facets (*Andò et al., 2012*).

361 A principal-component analysis (PCA; Fig. 5) was performed on the analyzed samples to highlight the
362 different controls on the tHM suites. Dimension 1, explaining around 43% of the compositional
363 variance, discriminates based on the different chemical durability of detrital minerals (*Garzanti et al.,*
364 *2018*) and thus chiefly reflects diagenesis of foreland-basin sediments. Dimension 2, explaining 18% of
365 the variance, discriminates between greenschist/blueschist minerals derived from the Alpine Internal
366 zone and amphibolite-facies minerals derived from higher-temperature Variscan metamorphic rocks

367 of the ECM or other minerals declining with deep burial as apatite and garnet (Garzanti et al., 2018),
 368 and thus mainly reflects sediment provenance.

369 In the PCA plot (Fig. 5), cave sands plot in the field of relatively fresh sediments, near modern
 370 sediments in streams draining the ECM. The Jalabres cave sand plots closer to the rivers draining the
 371 Ecrins-Pelvoux massif than the other caves, which plot in a more intermediate position between the
 372 Ecrins-Pelvoux massif and the Molasse deposits. This difference may point either to a larger
 373 contribution from the sedimentary cover of the external zone, or to more intense weathering
 374 conditions, in the Calvaire and Petit Odieux caves with respect to the Jalabres cave.

375



376

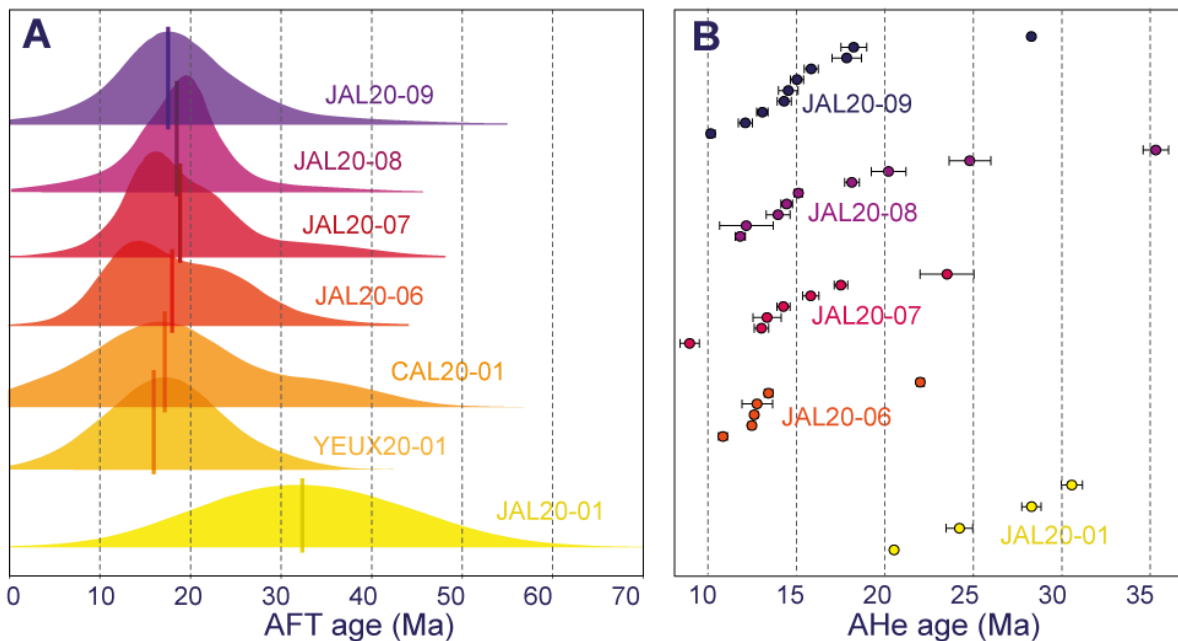
377 **Figure 5:** Principal component analysis (PCA) of transparent-heavy-mineral suites in cave sediments and modern
 378 river sands (including data from Garzanti et al., 2010). Ap = apatite + monazite, bl-g H = blue-green hornblende,
 379 g-br H = green-brown hornblende, &A = other amphiboles; Ep = epidote group, Grt = garnet, HgM = higher-grade
 380 metamorphic minerals (andalusite + kyanite + sillimanite + staurolite), LgM = lower-grade metamorphic minerals
 381 (prehnite + pumpellyite + chloritoid + lawsonite + carpholite), Px = pyroxenes, Ti& = anatase and titanite, ZTR =
 382 zircon + rutile + tourmaline (durable minerals).

383

384 4.3. Detrital thermochronology

385 Detailed AFT data (Table S4) and radial plots for each sample (generated using *RadialPlotter*;
386 *Vermeesch, 2009*) (Fig. S2) are available in the Supplementary material. All samples except JAL20-01
387 have central AFT ages between $15.9^{+3.5}_{-2.9}$ and $19.5^{+2.1}_{-1.9}$ Ma (Fig. 6A, Table S4); age distributions are
388 unimodal and show very little dispersion, even for sand samples (JAL20-07 and -08). The cobble sample
389 JAL20-01 stands out from the other JAL samples as it records a central AFT age of 32.3 ± 2.5 Ma. We
390 could measure 97 confined tracks on JAL samples (JAL20-06, -07, -08 and -09); combined, they show a
391 mean track length of $13.1 \pm 0.2 \mu\text{m}$ with a standard deviation of $2.2 \mu\text{m}$ (Fig. S3). The measured track
392 lengths are not correlated with D_{par} values, suggesting limited compositional control on track annealing
393 in these samples. The D_{par} value of sample JAL20-01 is slightly higher than for other JAL samples (1.90
394 $\pm 0.16 \mu\text{m}$ versus $1.55 \pm 0.22 \mu\text{m}$).

395 Single-grain AHe data are plotted in Figure 6B, with detailed analytical results given in the
396 Supplementary material (Table S5). The median AHe age for Jalabres cave samples is 14.4 Ma,
397 excepting sample JAL20-01, which yielded single-grain AHe ages between 20.5 and 30.6 Ma. No
398 correlation between single-grain AHe ages and effective uranium (eU) is observed in the dataset (Fig.
399 S4).



400
401 **Figure 6:** Detrital thermochronology results from the Obiou caves. **A:** Kernel density distributions of AFT single-
402 grain ages; vertical bars represent central AFT ages. **B:** Distributions of single-grain AHe ages for Jalabres cave
403 samples. See Supplementary material for full analytical data.

404

405 5. Data Interpretation and Discussion

406 5.1. Age and depositional environment

407 We obtained Serravalian – early Tortonian (10-13 Ma) ^{21}Ne - ^{10}Be burial ages for alluvial
408 sediments in the Jalabres cave (Fig. 3). These ages are consistent with the thermochronological data
409 from the same samples, which provide pre-depositional cooling ages from around 18 Ma (AFT) to 14
410 Ma (AHe). A Miocene burial age also explains the absence of measurable amounts of cosmogenic ^{26}Al
411 in all the cave samples.

412 *Jagercikova et al. (2022)* presented palynological results from a clay sample extracted from the
413 Petit Odieux cave, which, by comparison with results from the Western Alpine foreland (*Fauquette et*
414 *al., 2015*), suggest a Serravalian to earliest Zanclean age (i.e., ~5-14 Ma). Although broad, this age
415 range is consistent with our more precise TCN burial age of 11.5 ± 1.5 Ma. The pollen assemblage
416 includes both subtropical species, suggesting a low-elevation setting in a warmer-than-present mid- to
417 late-Miocene climate, and boreal species indicating that elevations >1900 m must have existed in the
418 region. *Jagercikova et al. (2022)* also report the occurrence of a small number of non-reworked
419 lagoonal and coastal dinoflagellates, suggesting that the caves formed in a coastal location close to
420 sea-level. Some cobbles show surface marks suggesting lithophagus perforations, which would confirm
421 deposition in a coastal environment. If confirmed, this observation would be crucial to constrain the
422 sea extent during mid- to late-Miocene times. Marine deposits of Serravillian-Tortonian age have been
423 found to the southwest of the Vercors (*Kalifi et al., 2021*), but constraints farther east remain scarce.
424 Assuming that the caves were formed close to sea level, they must have been uplifted to their present
425 elevation of 2300 m since 10-13 Ma. In addition, the Obiou summit is currently situated ~500 m above
426 the caves, providing an estimate for the minimum amount of topographic relief at the time of cave
427 formation.

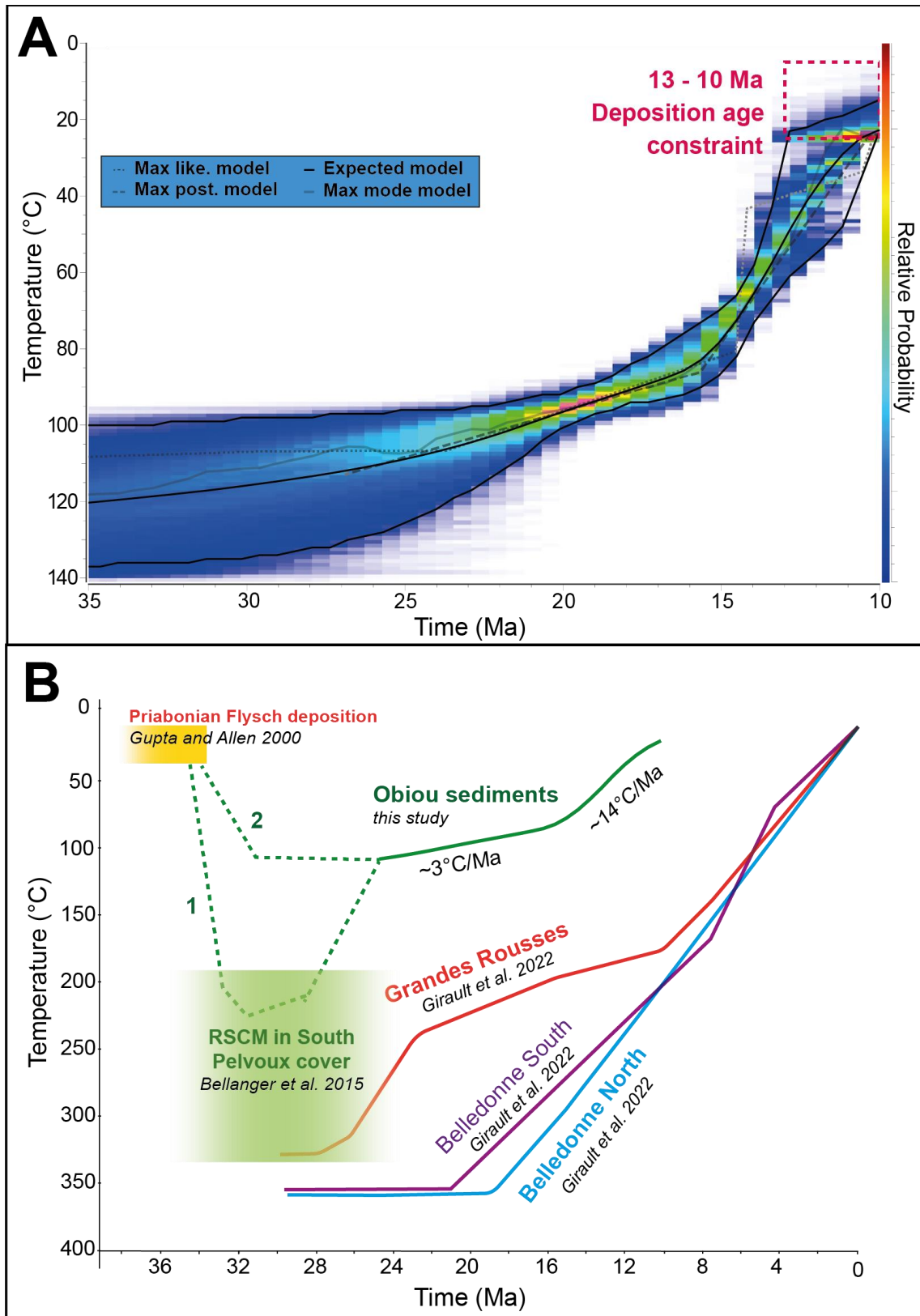
428 5.2. Incision and drainage development

429 The Jalabres cave is located ~1600 m above the modern Drac River (Fig. 1), providing evidence
430 for km-scale incision of the Drac since 10-13 Ma. The inferred integrated incision rate since
431 abandonment of the caves is of the order of 140 m/Ma. This rate is at least 5 times lower than late
432 Pleistocene – Holocene incision rates of the Drac and adjacent Buëch rivers, as inferred from TCN
433 dating of alluvial terraces (*Brocard et al., 2003*). A significant part of this incision may thus have taken
434 place since the onset of Quaternary glaciations, as reported elsewhere in the Western European Alps
435 (e.g., *Haeuselmann et al., 2007; Valla et al., 2011*).

436 The studied sediments from the Jalabres cave are clearly derived from the Ecrins-Pelvoux
437 massif (Figs. 4, 5). The deposits in the two other caves probably have a similar origin but show more
438 recycling and/or weathering. This provenance signal requires the existence of a radial drainage pattern
439 at 10-13 Ma, which was subsequently replaced by the current drainage system, separating the Dévoluy
440 massif from the Ecrins-Pelvoux massif by the axial Drac valley (Fig. 1B). The composition of the cave
441 deposits also clearly differs from that of the Oligocene molasse deposits in the Dévoluy massif, which
442 contain detritus from the Alpine internal zones that is absent in the cave deposits. The south-flowing
443 Durance River currently drains the internal zones of the Western Alps in this region (Fig. 1B). Thus,
444 these deposits provide evidence for two subsequent stages of drainage reorganization: (1) an
445 Oligocene radial drainage system that deposited the Dévoluy molasse extended to the internal zones;
446 the headwaters of this drainage system were cut off during the early Miocene by the establishment of
447 the axial upper Durance valley along the Penninic Frontal Thrust; and (2) the resulting shorter Late-
448 Miocene radial drainage network, with headwaters in the Ecrins-Pelvoux massif, was subsequently
449 reorganized into the current axial drainage with the establishment of the Drac valley. The first drainage
450 reorganization stage is coeval with reorganization of the upper Rhone and Rhine rivers in the Swiss
451 Alps (*Schlunegger et al., 1998*); these rivers are also in the same structural position as the upper
452 Durance, i.e., between the Aar ECM and the internal zones (Fig. 1).

453 *5.3. Thermal and exhumation history of the Ecrins-Pelvoux massif*

454 All samples except JAL20-01 provide similar AFT ages and track-length distributions with low
455 single-grain age dispersion, even for sand samples. This suggests that the cave samples registered a
456 uniform source-area exhumation history, consistent with the provenance data indicating sediment
457 sourcing from the Ecrins-Pelvoux massif. We employ inverse thermal-history modelling (using the
458 QTQt code; *Gallagher, 2012*) to infer time-temperature paths from the thermochronology data. We
459 used all available AHe and AFT data from the Jalabres cave (including track-length and Dpar data) as
460 input, and included as the sole temperature constraint that the samples must have been at surface
461 temperatures when they were deposited in the cave between 13 and 10 Ma. Our model outputs (Fig.
462 7A) predict slow cooling of ~ 3 °C/Ma between 24 and 15-16 Ma, increasing to >14 °C/Ma after that
463 time. Assuming a uniform geothermal gradient of ~ 30 °C/km, this thermal history is equivalent to an
464 exhumation rate increasing from ~ 0.1 km/Ma up to ~ 0.5 km/Ma.



465

466 **Figure 7: A.** Thermal history inferred from the Jalabres cave sediments, using available thermochronology data
 467 as input and TCN burial ages as an independent constraint on depositional age (red dotted box). Inferred
 468 temperature history is shown as relative probability (colours) with “best-fit” histories using different metrics and
 469 their 95% credible interval shown as black lines (see *Gallagher, 2012* for details). **B.** Comparison with regional

470 Time-temperature paths and constraints from the literature. The dotted lines represent two alternative scenarios
471 discussed in the text.

472

473 This inferred thermal history appears consistent with regional exhumation patterns (Fig. 7B)
474 as recorded by bedrock thermochronology in the Ecrins-Pelvoux and adjacent Grandes Rousses and
475 Belledonne massifs (*Seward et al., 1999; Tricart et al., 2007; van der Beek et al., 2010; Girault et al.,*
476 *2022*). These massifs record an onset or acceleration of exhumation during the early- to mid- Miocene,
477 between ~15 and 20 Ma (Fig. 7B). *Girault et al. (2022)* linked this acceleration to the transition from
478 distributed shortening to localized thrusting and uplift on crustal-scale ramps beneath the ECM. A
479 similar transition was recorded slightly earlier (20-22 Ma) in the Aar massif to the northeast (*Herwegh*
480 *et al., 2019*). Our new data provide tighter constraints on this Miocene acceleration of exhumation
481 rates for the Ecrins-Pelvoux massif.

482 The maximum burial temperature reached by the sedimentary cover of the Ecrins-Pelvoux
483 massif, before the onset of exhumation, is constrained by Raman spectroscopy of carbonaceous
484 material (RSCM; *Bellanger et al., 2015*), with values increasing from <200 °C in the southwest to ~350
485 °C in the central part of the massif. These temperatures record heating of the massif and its cover by
486 tectonic burial below the advancing Penninic Frontal Thrust (Fig. 1B) in the early Oligocene (*Simon-*
487 *Labric et al., 2009*). They also require rapid Oligocene cooling of the central Pelvoux massif, similar to
488 what is observed in the Grandes Rousses (Fig. 7B, path 1). In contrast, detrital zircon fission-track (ZFT)
489 ages from Priabonian flysch in the southern Pelvoux are older than the depositional ages, implying that
490 they were not, or only partially, reset (*Seward et al., 1999; Bernet, 2013*). The ZFT data thus imply
491 limited Oligocene reheating in the southern Pelvoux massif due to underthrusting beneath the
492 Penninic Front. This argues for a lower-temperature scenario (Fig. 7B, path 2), taking into account that
493 the source rocks for the sediments deposited in the cave at 10-13 Ma must have been situated
494 structurally above the currently exposed bedrock, and therefore recorded cooler conditions. Sample
495 JAL20-01 is the only sample to record Oligocene cooling, with an AFT central age of 32 Ma. It could
496 have derived from a now-eroded, partially-reset zone at high elevations in the Pelvoux basement.
497 Several single-grain AHe ages of ~29 Ma in sample YEUX20-01 may also indicate a contribution of
498 early-exhumed bedrock, fitting with scenario no. 2 of Fig. 7B.

499 The widespread exposure of Pelvoux basement rocks in mid-Miocene times, as suggested by
500 the petrography of the cave sediments, requires the structure and/or exhumation history of the Ecrins-
501 Pelvoux massif to be reconsidered. *Dumont et al. (2012)* proposed a geometrical reconstruction of the
502 basement-cover interface in the Ecrins-Pelvoux massif, which implied that the thickness of eroded

503 basement does not exceed 3 km in the most incised valleys. However, these valleys also record young
504 (3-5 Ma) AFT ages, implying considerable exhumation since that time, which appears inconsistent with
505 both early basement exposure and a missing basement section of only 3 km.

506 *5.4. A model for regional topographic and drainage-network evolution*

507 The Obiou cave sediments provide evidence for two successive drainage reorganizations: the
508 headwaters of a long radial drainage system, reaching into the internal zones, were beheaded by the
509 establishment of the axial upper Durance valley between the Oligocene and the mid-Miocene, and the
510 shorter radial drainage sourced in the Ecrins-Pelvoux massif was replaced by the axial Drac valley
511 during the late Miocene. The timing of the first reorganization is coeval with the acceleration of
512 exhumation in the Ecrins-Pelvoux massif, which has been linked to the onset of localized thrusting on
513 a crustal-scale ramp (*Girault et al., 2022*). This basement thrust would correspond to the Alpine frontal
514 thrust (Fig. 8) identified on the nearby CIFALP seismic profile as a major crustal discontinuity (*Nouibat
515 et al., 2022*). We suggest that thrusting over this ramp induced surface uplift of the Ecrins-Pelvoux
516 massif and split the former drainage network (Fig. 8). Such a tectonically driven process of drainage
517 deflection corresponds to a classical concept documented in various contexts, including the Zagros
518 Mountains and the Appalachians (*Oberlander and Morisawa, 1985*), the Siwaliks (*van der Beek et al.,
519 2002*), and the Aar massif in the external zone of the Swiss Alps (*Schlunegger et al., 1998; Kühni and
520 Pfiffner, 2001*).

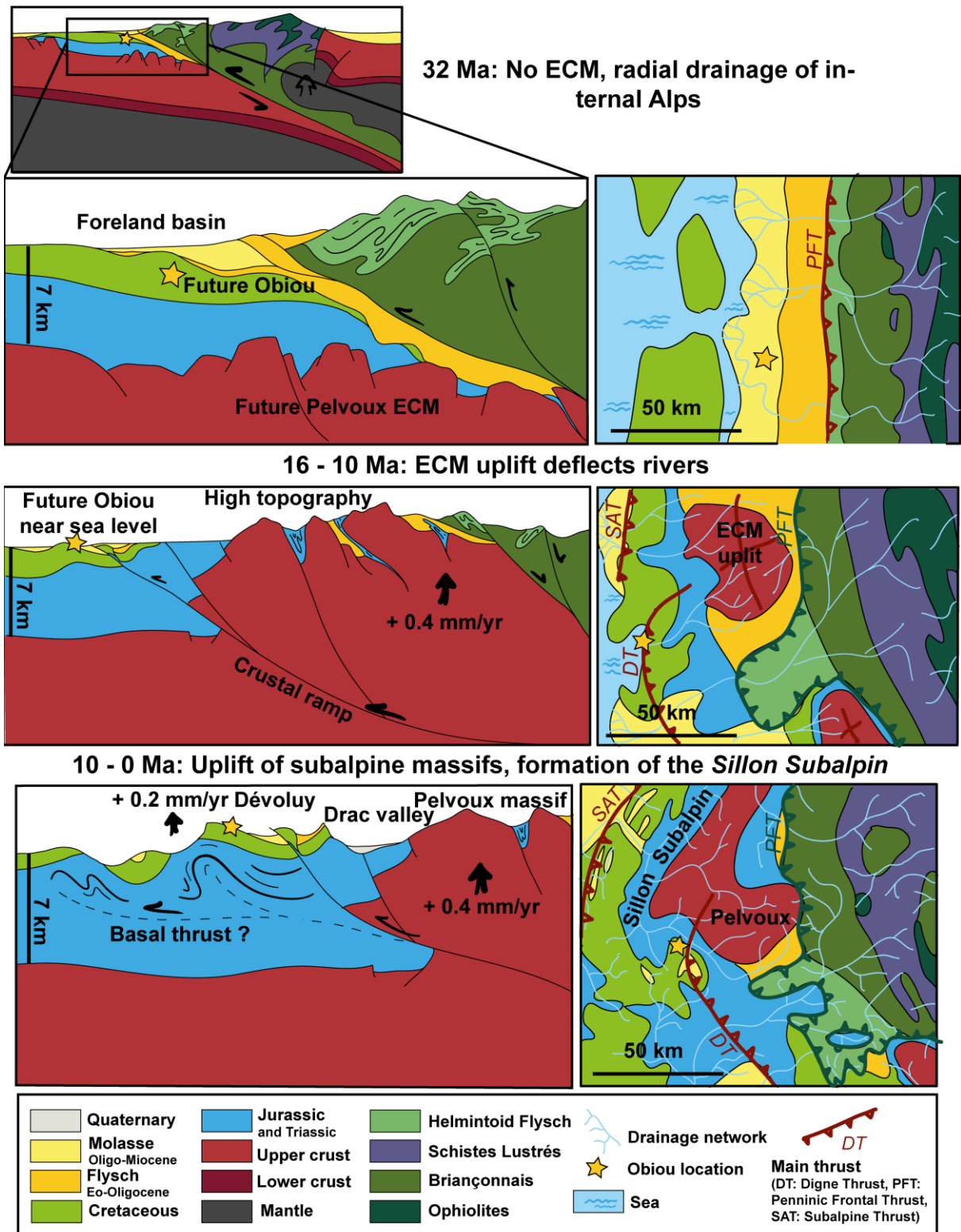
521 A similar model applies to the modern drainage system that is deflected around the Subalpine
522 Chartreuse, Vercors and Dévoluy massifs (Fig. 1). Steep thrusts in these Subalpine massifs were active
523 during Miocene times and propagated outward (*Kalifi et al., 2022; Bilau et al., in review.*). Initial
524 thrusting in the eastern Dévoluy massif during the middle Miocene would have uplifted the Jalabres
525 cave area above sea level, created the inferred ~500 m of local relief, induced erosion of most of the
526 molasse cover deposits, and started speleogenesis. Continued thrusting and uplift of the Subalpine
527 massifs probably controlled the formation of the axial drainage of the “*Sillon Subalpin*” since ~10 Ma.
528 The “*Sillon Subalpin*” terminates at the middle Durance valley to the south of the Dévoluy massif, and
529 we suggest that both the lack of resistant lithologies and the flat décollement layer under the Digne
530 nappe explains the preservation of the radial drainage network in the southern part of the Western
531 European Alps. These new findings contribute to resolving a long-standing controversy on the origin
532 of these axial valleys of the French Western Alps and the timing of their incision (*Blanchard, 1947;
533 Debelmas, 1995*). Glacial carving of the “*Sillon Subalpin*” occurred preferentially in soft upper-Jurassic
534 marls that were, according to *Debelmas (1995)*, exposed after a supposed peneplanation phase.
535 However, such a peneplanation phase appears inconsistent with our new data on the Miocene

536 paleotopography; we show that significant relief existed prior to axial-valley development and the
537 modern drainage formed during the Miocene in response to tectonic activity.

538 6. Conclusions

539 The Obiou cave system provides a rare long paleo-environmental and geodynamic record from
540 an intra-orogenic setting, formed in a karstic environment during mid- to late-Miocene times. Our
541 analyses of the preserved cave sediments, which were sourced from the nearby Ecrins-Pelvoux ECM,
542 provides new constraints on the Neogene structural, topographic and drainage evolution of this part
543 of the Western Alps.

544 The alluvial sediments from the Jalabres cave yield TCN burial ages of 11.5 ± 1.5 Ma. The
545 existence of sediments derived from the Ecrins-Pelvoux massif in the Dévoluy massif has implications
546 for both the timing of drainage rearrangement and the long-term incision rate of the Drac valley, which
547 is estimated around 140 m/My. Detrital thermochronology of the cave sediments records early
548 exhumation of the Ecrins-Pelvoux massif with an unprecedented resolution. The increase in
549 exhumation rate from 0.1 to 0.5 km/My just after 15-16 Ma may coincide with the activation of a
550 crustal-scale thrust and can be linked to surface uplift leading to high topography in the Ecrins-Pelvoux
551 massif. Consequently, the regional drainage network was reorganized, with a major change in
552 sediment sources during the Miocene from the Internal to the External zones of the Western French
553 Alps. Subsequent thrusting in the Subalpine massifs during the Late Miocene led to a second drainage
554 rearrangement and the development of the modern axial drainage system.



556

557 **Figure 8:** Tectonic, topographic and drainage development of the western Alps in the vicinity of the Ecrins-
 558 Pelvoux and Dévoluy massifs. Cross-sections and maps show three stages of evolution, from top to bottom:
 559 Oligocene (*Jourdan et al., 2012; Fauquette et al. 2015*), middle-late Miocene (as inferred from cave sediments),
 560 and modern setting.

561 **Acknowledgments**

562 The authors warmly thank V. Mai Yung Sen and A. de Leeuw for help in the field, F. Coeur and F.
563 Senebier (GTC platform) for help during sample processing, the ASTER team for the measurements
564 performed at the ASTER AMS facility (CEREGE, Aix-en-Provence), E. Schnabel (GFZ) for performing the
565 noble gas analyses, and the ISTERre TRB team for discussion. This study was supported by the French
566 ANR-PIA program (ANR-18-MPGA-0006) and internal BQR funding from ISTERre. All data are available
567 in tables in the main text and online supporting information.

568

569 **Appendix A. Supplementary data**

570 Supplementary data to this article can be found online at XXX.

571

572 **References**

- 573 Allen, P.A., From landscapes into geological history. *Nature* 451, 274–276, doi: 10.1038/nature06586, 2008.
- 574 Audra, P. and A. N. Palmer, The pattern of caves: controls of epigenic speleogenesis. *Géomorphologie: relief, processus,*
575 *environnement*, 17 (4), 359-378, doi: [10.4000/geomorphologie.9571](https://doi.org/10.4000/geomorphologie.9571), 2011.
- 576 Andò, S., E. Garzanti, M. Padoan, M. and Limonta, Corrosion of heavy minerals during weathering and diagenesis: A catalog
577 for optical analysis. *Sedimentary Geology*, 280, 165–178, 10.1016/j.sedgeo.2012.03.023, 2012.
- 578 Andò, S., Gravimetric separation of heavy minerals in sediments and rocks. *Minerals*, 10 (3), 273, doi: 10.3390/min10030273,
579 2020.
- 580 Arnold M., S. Merchel, D. L. Bourlès, R. Braucher, L. Benedetti, R. C. Finkel, G. Aumaître, A. Gott dang, M. Klein, The French
581 accelerator mass spectrometry facility ASTER: Improved performance and developments, *Nuclear Instruments and Methods*
582 *in Physics Research Section B: Beam Interactions with Materials and Atoms*, 268 (11–12), 1954-1959, doi:
583 10.1016/j.nimb.2010.02.107, 2010.
- 584 Bellanger, M., R. Augier, N. Bellahsen, L. Jolivet, P. Monié, T. Baudin, and O. Beyssac, Shortening of the European Dauphinois
585 margin (Oisans Massif, Western Alps): New insights from RSCM maximum temperature estimates and ⁴⁰Ar/³⁹Ar in situ dating,
586 *Journal of Geodynamics*, 83, 37–64, doi: 10.1016/j.jog.2014.09.004, 2015.
- 587 Bernet, M., Detrital zircon fission-track thermochronology of the present day Isère River drainage system in the Western Alps:
588 No evidence for increasing erosion rates at 5 Ma, *Geosciences*, 3 (3), 528–542, doi: 10.3390/geosciences3030528, 2013.
- 589 Beucher, R., P. van der Beek, J. Braun, and G. E. Batt, Exhumation and relief development in the Pelvoux and Dora-Maira
590 massifs (Western Alps) assessed by spectral analysis and inversion of thermochronological age transects, *Journal of*
591 *Geophysical Research: Earth Surface*, 117 (F3), doi: 10.1029/2011JF002240, 2012.
- 592 Blanchard R., *Les Alpes occidentales*, II, Les cluses préalpines et le sillon alpin, 672 p., Arthaud, 1947.

593 Blard P.-H., M. Lupker, M. Rousseau, and J. Tesson, Two MATLAB programs for computing paleo-elevations and burial ages
594 from paired-cosmogenic nuclides. *MethodsX*, 6, 1547-1556, doi: 10.1016/j.mex.2019.05.017, 2019.

595 Bocquet, J., Le delta miocène de Voreppe. Etude des faciès conglomératiques du Miocène des environs de Grenoble, *Travaux*
596 *du Laboratoire de Géologie de l'Université de Grenoble*, 42, 53–75, 1966.

597 Braucher, R., V. Guillou, D. Bourlès, M. Arnold, G. Aumaître, K. Keddadouche, and E. Nottoli, Preparation of ASTER in-house
598 $^{10}\text{Be}/^9\text{Be}$ standard solutions, *Nuclear Instruments and Methods in Physics Research Section B: Beam Interactions with*
599 *Materials and Atoms*, 361, 335–340, doi: 10.1016/j.nimb.2015.06.012, 2015.

600 Brocard G.Y., P.A. van der Beek, D.L. Bourlès, L.L. Siame, J.-L. Mugnier, Long-term fluvial incision rates and postglacial river
601 relaxation time in the French Western Alps from ^{10}Be dating of alluvial terraces with assessment of inheritance, soil
602 development and wind ablation effects, *Earth and Planetary Science Letters*, 209 (1–2), 197-214, doi: 10.1016/S0012-
603 821X(03)00031-1, 2003.

604 Craw, D., Upton, P., Burridge, C.P., Wallis, G.P., Waters, J.M., Rapid biological speciation driven by tectonic evolution in New
605 Zealand. *Nature Geoscience* 9, 140–144, doi: 10.1038/ngeo2618, 2016.

606 Crouzet, C., G. Ménard, and P. Rochette, P., 2001, Cooling history of the Dauphinoise Zone (Western Alps, France) deduced
607 from the thermopaleomagnetic record: geodynamic implications. *Tectonophysics*, 340, 79-93, 2001.

608 Debelmas, J., Le creusement du Grésivaudan: état actuel du problème, *Géologie alpine*, 71, 169–173, 1995.

609 Dingle, E. H., M. Attal, and H. D. Sinclair, Abrasion-set limits on Himalayan gravel flux, *Nature*, 544 (7651), 471–474, doi:
610 10.1038/nature22039, 2017.

611 Dumont, T., S. Schwartz, S. Guillot, T. Simon-Labric, P. Tricart, and S. Jourdan, Structural and sedimentary records of the
612 Oligocene revolution in the Western Alpine arc, *Journal of Geodynamics*, 56-57, 18–38, doi: 10.1016/j.jog.2011.11.006,
613 geodynamics and Orogenesis, 2012.

614 Fauquette, S., M. Bernet, J.-P. Suc, A.-S. Grosjean, S. Guillot, P. van der Beek, S. Jourdan, S.-M. Popescu, G. Jiménez-Moreno,
615 A. Bertini, B. Pittet, P. Tricart, T. Dumont, S. Schwartz, Z. Zheng, E. Roche, G. Pavia, and V. Gardien, Quantifying the Eocene to
616 Pleistocene topographic evolution of the southwestern Alps, France and Italy, *Earth and Planetary Science Letters*, 412, 220–
617 234, doi: 10.1016/j.epsl.2014.12.036, 2015.

618 Gallagher, K., Transdimensional inverse thermal history modeling for quantitative thermochronology, *J. Geophys. Res.*, 117
619 (B2), 408, doi:10.1029/2011JB008825, 2012.

620 Garzanti, E., Petrographic classification of sand and sandstone, *Earth-Science Reviews* 192, 545-563, doi:
621 10.1016/j.earscirev.2018.12.014, 2019.

622 Garzanti, E., and Andò, S., Heavy minerals for junior woodchucks. *Minerals*, 9(3), 148, doi: 10.3390/min9030148, 2019.

623 Garzanti, E., S. Andò, M. Limonta, L. Fielding, and Y. Najman, Diagenetic control on mineralogical suites in sand, silt, and mud
624 (Cenozoic Nile Delta): Implications for provenance reconstructions, *Earth-Science Reviews*, 185, 122-139, doi:
625 10.1016/j.earscirev.2018.05.010, 2018.

626 Garzanti, E., Resentini, A., Vezzoli, G., Ando, S., Malusa, M.G., Padoan, M. and Paparella, P., Detrital fingerprints of fossil
627 continental-subduction zones (Axial Belt Provenance, European Alps), *The Journal of Geology*, 118(4), pp.341-362, doi:
628 10.1086/652720, 2010.

629 Girault J.B., N. Bellahsen, M. Bernet, R. Pik, N. Loget, E. Lasseur, C.L. Rosenberg, M. Balvay, and M. Sonnet, Exhumation of the
630 Western Alpine collisional wedge: New thermochronological data, *Tectonophysics*, 822, 229155, doi:
631 10.1016/j.tecto.2021.229155, 2022.

632 Glotzbach, C., van der Beek, P.A., and Spiegel, C., Episodic exhumation and relief growth in the Mont Blanc massif, Western
633 Alps from numerical modelling of thermochronology data. *Earth and Planetary Science Letters*, 304, 417–430, doi:
634 10.1016/j.epsl.2011.02.020, 2011b.

635 Glotzbach, C., M. Bernet, and P. van der Beek, Detrital thermochronology records changing source areas and steady
636 exhumation in the Western European Alps, *Geology*, 39 (3), 239–242, doi:10.1130/G31757.1, 2011a.

637 Granger, D.E., and Muzikar, P.F., Dating sediment burial with in situ-produced cosmogenic nuclides: theory, techniques, and
638 limitations. *Earth and Planetary Science Letters*, 188, 269–281. doi: [10.1016/S0012-821X\(01\)00309-0](https://doi.org/10.1016/S0012-821X(01)00309-0), 2001.

639 Gupta, S., and P. A. Allen, Implications of foreland paleotopography for stratigraphic development in the Eocene distal Alpine
640 foreland basin. *Geological Society of America Bulletin*, 112 (4), 515–530, doi: 10.1130/0016-
641 7606(2000)112<515:IOFPFS>2.0.CO;2, 2000.

642 Haeuselmann, P., D. E. Granger, P.-Y. Jeannin, and S.-E. Lauritzen, Abrupt glacial valley incision at 0.8 Ma dated from cave
643 deposits in Switzerland, *Geology*, 35 (2), 143–146, doi: 10.1130/G23094A, 2007.

644 Herwegh, M., Berger, A., Glotzbach, C., Wangenheim, C., Mock, S., Wehrens, P., Baumberger, R., Egli, D., and Kissling, E., Late
645 stages of continent-continent collision: timing, kinematic evolution, and exhumation of the northern rim (Aar Massif) of the
646 Alps. *Earth-Science Reviews*, 200, 102959. <https://doi.org/10.1016/j.earscirev.2019.102959>, 2019.

647 Hetzel, R., S. Niedermann, S Ivy-Ochs, P. W. Kubik, M. Tao, B. Gao, ²¹Ne versus ¹⁰Be and ²⁶Al exposure ages of fluvial terraces:
648 the influence of crustal Ne in quartz, *Earth and Planetary Science Letters*, 201, 575-591, doi: 10.1016/S0012-821X(02)00748-
649 3, 2002.

650 Hurford, J. A., and P. F. Green, The zeta age calibration of fission-track dating, *Chemical Geology*, 41, 285-317, doi:
651 10.1016/S0009-2541(83)80026-6, 1983.

652 Jagercikova, M., L. Mocochain, A.-E. Lebatard, D. Bourlès, L. Leanni, A. Sartégou, and A. Zappelli, Découverte et étude de
653 remplissages karstiques allochtones d'âge miocène dans l'Obiou (Dévoluy, Alpes françaises) Implications géomorphologiques
654 et paléogéographiques, *Karstologia*, 77, 49-62, 2021.

655 Jagercikova, M, F. Lemot, P. Valla, S.-P. Popescu, S. Fauquette, J.-P. Suc, A. Sartegou, P. van der Beek, L. Mocochain, and A.
656 Zapelli, Relief and paleo-environmental conditions during the mid-late Miocene in the French Western Alps (Dévoluy Massif)
657 revealed by Obiou cave deposits, 18th Int. Congress of Speleology – Symposium 3, 2022.

658 Jourdan, S., M. Bernet, S. Schwartz, S. Guillot, P. Tricart, C. Chauvel, T. Dumont, G. Montagnac, and S. Bureau, Tracing the
659 Oligocene-Miocene evolution of the western Alps drainage divide with pebble petrology, geochemistry, and Raman
660 spectroscopy of foreland basin deposits, *The Journal of Geology*, 120(6), 603–624, doi: 10.1086/667813, 2012.

661 Kalifi, A., P. Sorrel, P.-H. Leloup, A. Galy, V. Spina, B. Huet, S. Russo, B. Pittet, and J.-L. Rubino, Tectonic control on the
662 paleogeographical seaway along the Western Alpine foreland basin, *Geological Society London Special Publications*, 523, doi:
663 10.1144/SP523-2021-78, 2022.

664 Kalifi, A., P.-H. Leloup, P. Sorrel, A. Galy, F. demory, V. Spina, B. Huet, F. Quillévéré, F. Ricciardi, D. Michoux, K. Lecacheur, R.
665 Grime, B. Pittet, and J-L. Rubino, Chronology of thrust propagation from an updated tectono-sedimentary framework of the
666 Miocene molasse (western Alps), *Solid Earth*, 12, 2735-2771, doi: 10.5194/se-12-2735-2021, 2021.

667 Kober, F., V. Alfimov, S. Ivy-Ochs, P. Kubik, and R. Wieler, The cosmogenic ^{21}Ne production rate in quartz evaluated on a large
668 set of existing ^{21}Ne – ^{10}Be data, *Earth and Planetary Science Letters*, 302 (1), 163–171, doi: 10.1016/j.epsl.2010.12.008, 2011

669 Kuhlemann, J., and Kempf, O., Post-Eocene evolution of the North Alpine Foreland Basin and its response to Alpine tectonics.
670 *Sedimentary Geology*, 152, 45–78. doi: [10.1016/S0037-0738\(01\)00285-8](https://doi.org/10.1016/S0037-0738(01)00285-8), 2002.

671 Kuhlemann, J., Dunkl, I., Brugel, A., Spiegel, C., and Frisch, W., From source terrains of the eastern Alps to the Molasse Basin:
672 Detrital record of non-steady-state exhumation: *Tectonophysics*, v. 413, p. 301–316, doi:10.1016/j.tecto.2005.11.007, 2006.

673 Kühni, A., and O. A. Pfiffner, Drainage patterns and tectonic forcing: a model study for the Swiss alps, *Basin Research*, 13 (2),
674 169–197, doi: 10.1046/j.1365-2117.2001.00146.x, 2001.

675 Lal, D., Cosmic ray labeling of erosion surfaces: in situ nuclide production rates and erosion models, *Earth and Planetary
676 Science Letters*, 104, 424-439,doi: 10.1016/0012-821X(91)90220-C, 1991

677 Ma, Y., W. Wang, D. Zheng, H. Zhang, J. Pang, Y. Wu, F. M. Stuart, and S. Xu, Mid-Miocene cosmogenic upper limit for $^{10}\text{Be}/^{21}\text{Ne}$
678 burial age, *Quaternary Geochronology*, 48, 72–79, doi: 10.1016/j.quageo.2018.08.004, 2018.

679 Malcles, O., P. Vernant, J. Chéry, J.-F. Ritz, G. Cazes, and D. Fink, Âges d'enfouissement, fantômes de roches et structuration
680 karstique, cas de la vallée de la Vis (Sud de la France), *Géomorphologie : relief, processus, environnement*, 26 (4), 255–264,
681 doi: 10.4000/geomorphologie.15043, 2020.

682 Mariotti, A., P.-H. Blard, J. Charreau, C. Petit, S. Molliex, and the ASTER Team, Denudation systematics inferred from in situ
683 cosmogenic ^{10}Be concentrations in fine (50–100 μm) and medium (100–250 μm) sediments of the Var River basin, southern
684 French Alps, *Earth Surface Dynamics*, 7(4), 1059–1074, doi: 10.5194/esurf-7-1059-2019, 2019.

685 Martin, L.C.P., P.-H. Blard, G. Balco, J. Lavé, R. Delunel, N. Lifton, and V. Laurent, The CREp program and the ICE-D production
686 rate calibration database: A fully parameterizable and updated online tool to compute cosmic-ray exposure ages, *Quaternary
687 Geochronology*, 38, 25-49, doi: 10.1016/j.quageo.2016.11.006, 2017.

688 Masini, E., Manatschal, G., and Mohn, G., The Alpine Tethys rifted margins: Reconciling old and new ideas to understand the
689 stratigraphic architecture of magma-poor rifted margins. *Sedimentology*, 60, 174–196, doi: [10.1111/sed.12017](https://doi.org/10.1111/sed.12017), 2013.

690 McPhillips, D., G. D. Hoke, J. Liu-Zeng, P. R. Bierman, D. H. Rood, and S. Niedermann, Dating the incision of the Yangtze River
691 gorge at the First Bend using three-nuclide burial ages, *Geophysical Research Letters*, 43 (1), 101–110, doi:
692 10.1002/2015GL066780, 2016.

693 Meckel, L. D., Sedimentological and structural evolution of the Tertiary Dévoluy basin, external Western Alps, SE France, Ph.D.
694 thesis, ETH Zurich, 1997.

695 Merchel, S., and U. Hergers, An update on radiochemical separation techniques for the determination of long-lived
696 radionuclides via accelerator mass spectrometry, *Radiochimica Acta*, 84(4), 215–220, doi: 10.1524/ract.1999.84.4.215, 1999

697 Monjuvent, G., Le Drac: Morphologie, stratigraphie et chronologie quaternaire d'un bassin alpin, Centre National de la
698 Recherche Scientifique, 421 pp, 1978.

699 Niedermann, S., Cosmic-ray-produced noble gases in terrestrial rocks: Dating tools for surface processes, *Reviews in*
700 *Mineralogy and Geochemistry*, 47 (1), 731–784, doi: 10.2138/rmg.2002.47.16, 2002.

701 Nouibat A., L. Stehly, A. Paul, S. Schwartz, T. Bodin, T. Dumont, Y. Rolland, R. Brossier, Cifalps Team and
702 AlpArray Working Group, Lithospheric transdimensional ambient-noise tomography of W-Europe: implications for crustal-
703 scale geometry of the W-Alps, *Geophysical Journal International*, 229 (2), 862–879, doi: 10.1093/gji/ggab520, 2022.

704 Oberlander, T., and M. Morisawa, Origin of drainage transverse to structures in orogens, *Tectonic geomorphology*,
705 *Proceedings of the 15th Annual Binghampton Geomorphological Symposium*, 155–182, 1985.

706 Philippe, Y., E. Deville, and A. Mascle, Thin-skinned inversion tectonics at oblique basin margins: example of the western
707 Vercors and Chartreuse Subalpine massifs (SE France). *Geological Society, London, Special Publications*, 134, 239–262.
708 <https://doi.org/10.1144/gsl.sp.1998.134.01.11>, 1998. Rosenbaum, G., and G. S. Lister, The Western Alps from the Jurassic to
709 Oligocene: spatio-temporal constraints and evolutionary reconstructions, *Earth-Science Reviews*, 69 (3), 281–306, doi:
710 10.1016/j.earscirev.2004.10.001, 2005.

711 Sauro, F., M. G. Fellin, A. Columbu, P. Häuselmann, A. Borsato, C. Carbone, and J. D. Waele, Hints on the late Miocene evolution
712 of the Tonale-Adamello-Brenta Region (Alps, Italy) based on allochthonous sediments from Raonzolo cave, *Frontiers in Earth*
713 *Sciences*, 9, doi: 10.3389/feart.2021.672119, 2021.

714 Sartégou, A., D. L. Bourlès, P.-H. Blard, R. Braucher, B. Tibari, L. Zimmermann, L. Leanni, G. Aumaître, and K. Keddadouche,
715 Deciphering landscape evolution with karstic networks: A Pyrenean case study, *Quaternary Geochronology*, 43, 12–29, doi:
716 10.1016/j.quageo.2017.09.005, 2018.

717 Schlunegger, F., Slingerland, R., and Matter, A., Crustal thickening and crustal extension as controls on the evolution of the
718 drainage network of the central Swiss Alps between 30 Ma and the present: constraints from the stratigraphy of the North
719 Alpine Foreland Basin and the structural evolution of the Alps. *Basin Research*, 10, 197–212, [doi: 10.1046/j.1365-](https://doi.org/10.1046/j.1365-2117.1998.00063.x)
720 [2117.1998.00063.x](https://doi.org/10.1046/j.1365-2117.1998.00063.x), 1998.

721 Schwartz, S., C. Gautheron, L. Audin, T. Dumont, J. Nomade, J. Barbarand, R. Pinna-Jamme, and P. van der Beek, Foreland
722 exhumation controlled by crustal thickening in the Western Alps, *Geology*, 45(2), 139–142, doi: 10.1130/G38561.1, 2017.

723 Seward, D., M. Ford, J. Bürgisser, H. Lickorish, E. Williams, and L. Meckel III, Preliminary results of fission-track analyses in the
724 southern Pelvoux area, SE France, *Memorie di Scienze Geologiche Padova*, 51, 25–31, 1999.

725 Simon-Labric, T., Y. Rolland, T. Dumont, T. Heymes, C. Authemayou, M. Corsini, and M. Fornari, ⁴⁰Ar/³⁹Ar dating of Penninic
726 Front tectonic displacement (W Alps) during the Lower Oligocene (31–34 Ma), *Terra Nova*, 21 (2), 127–136, doi:
727 10.1111/j.1365-3121.2009.00865.x, 2009.

728 Sternai, P., C. Sue, L. Husson, E. Serpelloni, T. W. Becker, S. D. Willett, C. Faccenna, A. Di Giulio, G. Spada, L. Jolivet, P. Valla,
729 C. Petit, J.-M. Nocquet, A. Walpersdorf, and S. Castelltort, Present-day uplift of the European Alps: Evaluating mechanisms
730 and models of their relative contributions, *Earth-Science Reviews*, 190, 589–604, doi: 10.1016/j.earscirev.2019.01.005, 2019.

731 Tricart, P., P. van der Beek, S. Schwartz, and E. Labrin, Diachronous late-stage exhumation across the western Alpine arc:
732 constraints from apatite fission-track thermochronology between the Pelvoux and Dora-Maira Massifs, *Journal of the*
733 *Geological Society*, 164 (1), 163–174, doi:10.1144/0016-76492005-174, 2007.

734 Valla, P. G., Shuster, D. L., and van der Beek, P. A., Significant increase in relief of the European Alps during mid-Pleistocene
735 glaciations, *Nat. Geosci.*, 4, 688–692, doi:10.1038/ngeo1242, 2011.

736 Valla, P. G., Sternai, P., and Fox, M.: How Climate, Uplift and Erosion Shaped the Alpine Topography, *Elements*, 17, 41–46,
737 doi:10.2138/gselements.17.1.41, 2021.

738 van der Beek, P., B. Champel, and J.-L. Mugnier, Control of detachment dip on drainage development in regions of active
739 fault-propagation folding, *Geology*, 30 (5), 471–474, doi: 10.1130/0091-7613(2002)030<0471:CODDOD>2.0.CO;2, 2002.

740 van der Beek, P. A., P. G. Valla, F. Herman, J. Braun, C. Persano, K. J. Dobson, and E. Labrin, Inversion of thermochronological
741 age – elevation profiles to extract independent estimates of denudation and relief history — II: Application to the French
742 Western Alps, *Earth and Planetary Science Letters*, 296 (1), 9–22, doi: 10.1016/j.epsl.2010.04.032, 2010.

743 Vermeesch P., G. Balco, P.-H. Blard, T. J. Dunai, F. Kober, S. Niedermann, D. L. Shuster, S. Strasky, F. M. Stuart, R. Wieler, L.
744 Zimmermann, Interlaboratory comparison of cosmogenic ²¹Ne in quartz, *Quaternary Geochronology*, Volume 26, 2015,
745 Pages 20-28, <https://doi.org/10.1016/j.quageo.2012.11.009>, 2015.

746 Vermeesch, P., RadialPlotter: a Java application for fission track, luminescence and other radial plots, *Radiation*
747 *Measurements*, 44, 4, 409-410, 2009.

748 Whipple, K.X., Kirby, E., and Brocklehurst, S.H., Geomorphic limits to climate-induced increases in topographic relief. *Nature*,
749 401, 39–43, doi: 10.1038/43375, 1999.

750 Zhou, R., Schoennohm, L.M., Sobel, E.R., Davis, D.W., Glodny, J., New constraints on orogenic models of the southern Central
751 Andean Plateau: Cenozoic basin evolution and bedrock exhumation. *Geol. Soc. Am. Bull.* 129, 152–170. Doi:
752 10.1130/B31384.1, 2017.